AGU PUBLICATIONS

JGR

Journal of Geophysical Research: Solid Earth

RESEARCH ARTICLE
10.1002/2017JB013965

Key Points:
- We conducted high-frequency receiver function inversion using data from ocean bottom seismometers
- Multiple phases from a sediment and seawater columns were fully taken into consideration
- We revealed thin low-velocity layer along subducting plate which is considered as fluid-rich sediment layer

Supporting Information:
- Supporting Information S1

Correspondence to:
T. Akuhara,
akuhara@eri.u-tokyo.ac.jp

Citation:
Akuhara, T., K. Mochizuki, H. Kawakatsu, and N. Takeuchi (2017), A fluid-rich layer along the Nankai trough megathrust fault off the Kii Peninsula inferred from receiver function inversion, *J. Geophys. Res. Solid Earth*, *122*, 6524–6537, doi:10.1002/2017JB013965.

Received 9 JAN 2017
Accepted 29 JUL 2017
Accepted article online 4 AUG 2017
Published online 18 AUG 2017

A fluid-rich layer along the Nankai trough megathrust fault off the Kii Peninsula inferred from receiver function inversion

Takeshi Akuhara[1], Kimihiro Mochizuki[1], Hitoshi Kawakatsu[1], and Nozomu Takeuchi[1]

[1]Earthquake Research Institute, The University of Tokyo, Tokyo, Japan

Abstract Investigation of fluid distribution along megathrust faults is an important issue, since the fluid affects frictional properties and thus slip behavior on faults. Scattered teleseismic phases, or receiver functions (RFs), have made significant contributions to understanding the fluid content of subducting plates beneath the onshore regions but have been rarely applied in offshore settings. In this study, we conducted receiver function inversion analysis to investigate detailed seismic properties near the megathrust fault using ocean bottom seismometers deployed off the Kii Peninsula, southwest Japan. RFs were calculated at high frequencies (up to 4 Hz), removing the effect of water reverberations from vertical component records. Our inversion was performed in two steps: first, we modeled sediment layer by a simple stacking method and then solved for deeper structure by a waveform inversion. The results indicate the presence of a thin low-velocity zone (LVZ) of a thickness of 0.2–1.2 km with a *S* wave velocity of 0.7–2.4 km/s along the plate interface. We interpret this LVZ as thin fluid-rich sediment layer between the overriding and subducting plates that acts as a pathway of fluid migration.

1. Introduction

Recent seismological studies have revealed the importance of fluid at the subduction system that may control slip behavior on megathrust faults [*Kodaira et al*., 2004; *Song et al*., 2009; *Zhao et al*., 2011; *Kimura et al*., 2012]. Elevated pore fluid pressure near the plate interface is considered to reduce the fault strength such that slips occur easily [*Scholz*, 1998]. Such fluid originates from subducting plates via the mechanical compaction and metamorphic dehydration of the incoming sediment at shallow depth and metamorphic dehydration of the oceanic crust at greater depths [*Hyndman and Peacock*, 2003]. Released fluid not only increases pore fluid pressure at the place of dehydration but also is carried vertically through relatively permeable media and laterally along impermeable barriers such as plate interfaces [*Hyndman et al*., 2015; *McCrory et al*., 2016].

Two different types of seismological experiments have been conducted to evaluate fluid distribution along subducting plates: active- and passive-source seismic surveys. Active-source seismic surveys have been conducted mainly for shallow subduction portions, usually located at offshore. Some of these studies have reported extremely strong *P*-to-*P* reflection phases from top of subducting plates [*Kodaira et al*., 2002; *Nedimović et al*., 2003; *Mochizuki et al*., 2005; *Bangs et al*., 2009; *Bell et al*., 2010]. Note that the amplitudes of *P*-to-*P* reflection phases have sensitivity to the impedance (product of *P* wave velocity and density) contrast. Therefore, the strong amplitudes which cannot be explained by typical impedance contrast of rocks are often interpreted as low-velocity zones (LVZs) hosting large amount of fluid content. High-frequency content of active sources enables resolution of fine-scale structure of order 100 m.

For greater subduction depths (i.e., onshore settings), scattered teleseismic waves or receiver functions (RFs) have been utilized to estimate fluid distributions. The method aims to retrieve *P*-to-*S* conversion phases from teleseismic *P* coda waves that provide constraints on the *S* wave velocity contrast. RF analyses have detected LVZs along the plate interface of subduction zones worldwide as layers sandwiched by negative RF amplitudes above and positive amplitudes below. These LVZs are commonly interpreted as hydrated oceanic crust because of their anomalously low *S* wave velocity (or high Poisson's ratio) [*Kawakatsu and Watada*, 2007; *Audet et al*., 2009; *Hansen et al*., 2012; *Kim and Clayton*, 2015]. Since most studies employ low-pass corner frequencies $<$1.0 Hz to avoid instability from deconvolution and complication of interpretation, spatial resolution of RF analysis is much coarser (1–10 km order) than that of active-source seismic surveys.

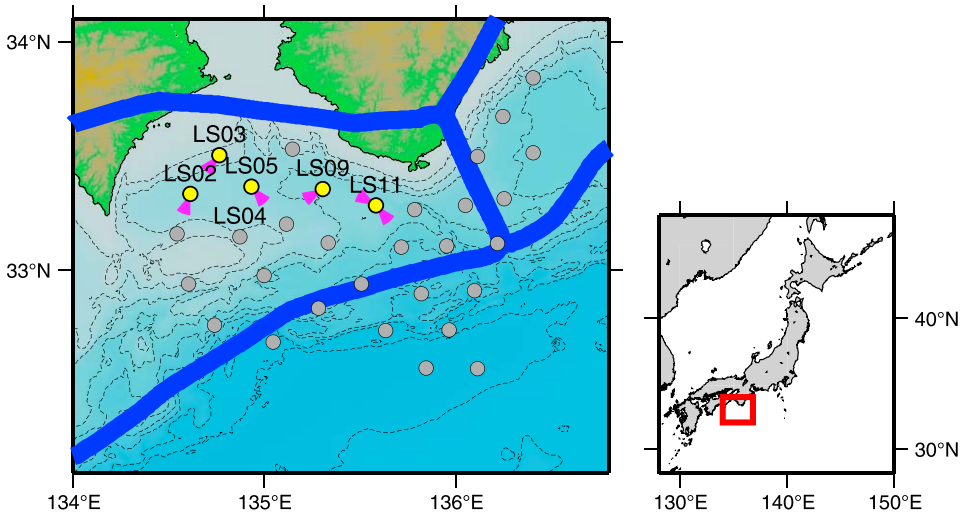

Figure 1. Tectonic setting of the study area and locations of ocean bottom seismometers (OBSs) (yellow and gray circles). Blue lines enclose the source regions of the 1944 Tonankai (to the east) and 1946 Nankai earthquakes (to the west). Five OBSs featured by this study are highlighted in yellow. Pink sectors show back azimuthal bins of teleseismic events to be analyzed. The location of the study area is enclosed by red rectangle in the right panel.

Since these two methods have different sensitivities, combining information obtained by both methods will lead to better understanding of megathrust faults. However, there are few applications of RF analysis to offshore setting to date. In addition, high-frequency analysis would be required so that the resolution of RF analysis can be comparable to that of active source surveys. Fortunately, such challenges can be addressed, because previous studies have found solutions to calculate RFs stably at high frequencies [*Park and Levin*, 2000, 2016] and with data recorded by ocean bottom seismometers (OBSs) where strong water reverberations dominate vertical component records [*Akuhara and Mochizuki*, 2015; *Akuhara et al*., 2016]. In this study, we perform RF analysis with OBSs deployed off the Kii Peninsula, located in southwest Japan to estimate seismic property of megathrust fault at seismogenic zone depth (Figure 1). The interface depth ($>$ 10 km) is somewhat difficult to investigate by active-source seismic surveys, so only a few studies have inferred its property [*Kodaira et al*., 2002].

2. High-Frequency Receiver Functions From OBS Records

Southwestern Japan subduction zone where the Philippine Sea Plate subducts hosts megathrust earthquakes with a cycle of about 100–150 years [*Ando*, 1975]. From November 2003 to December 2007, OBSs were deployed at 32 sites on the seafloor, crossing both source regions of the 1944 Tonankai and the 1946 Nankai earthquakes (Figure 1). The OBSs were equipped with three-component sensors that have natural frequency of 1 Hz. We calculated radial component RFs using these OBSs. We extracted three-component seismograms of teleseismic events ($M > 6.0$) at 30–90° distance from the OBS network and rotated horizontal components into radial and transverse directions. Signal-to-noise ratios (SNRs) were measured on the vertical component records to select data with clear *P* wave onsets (SNR $>$ 3.0).

Since the vertical component records suffer from dominant water reverberations, we applied inverse water layer filter (IWLF) to suppress them [*Akuhara and Mochizuki*, 2015; *Akuhara et al*., 2016]. The IWLF method requires two tuning parameters to be determined at each station (a two-way traveltime of *P* waves within the water column and a reflection coefficient on the seafloor). These parameters were determined by a nonlinear waveform inversion [*Akuhara et al*., 2016]. We inspected this process with IWLF by comparing autocorrelation functions of vertical component records before and after the application of IWLF and retained traces for which the IWLF suppressed water reverberations as expected (Text S1 in the supporting information). Finally, radial RFs were obtained by deconvolving the inverse water layer-filtered vertical component records from radial component records. We employed the extended-time multitaper method to operate the deconvolution [*Shibutani et al*., 2008]. The method has advantage in stable computation of RFs even at high frequency. We applied cosine-shaped low-pass filter to 4 Hz to the obtained radial RFs.

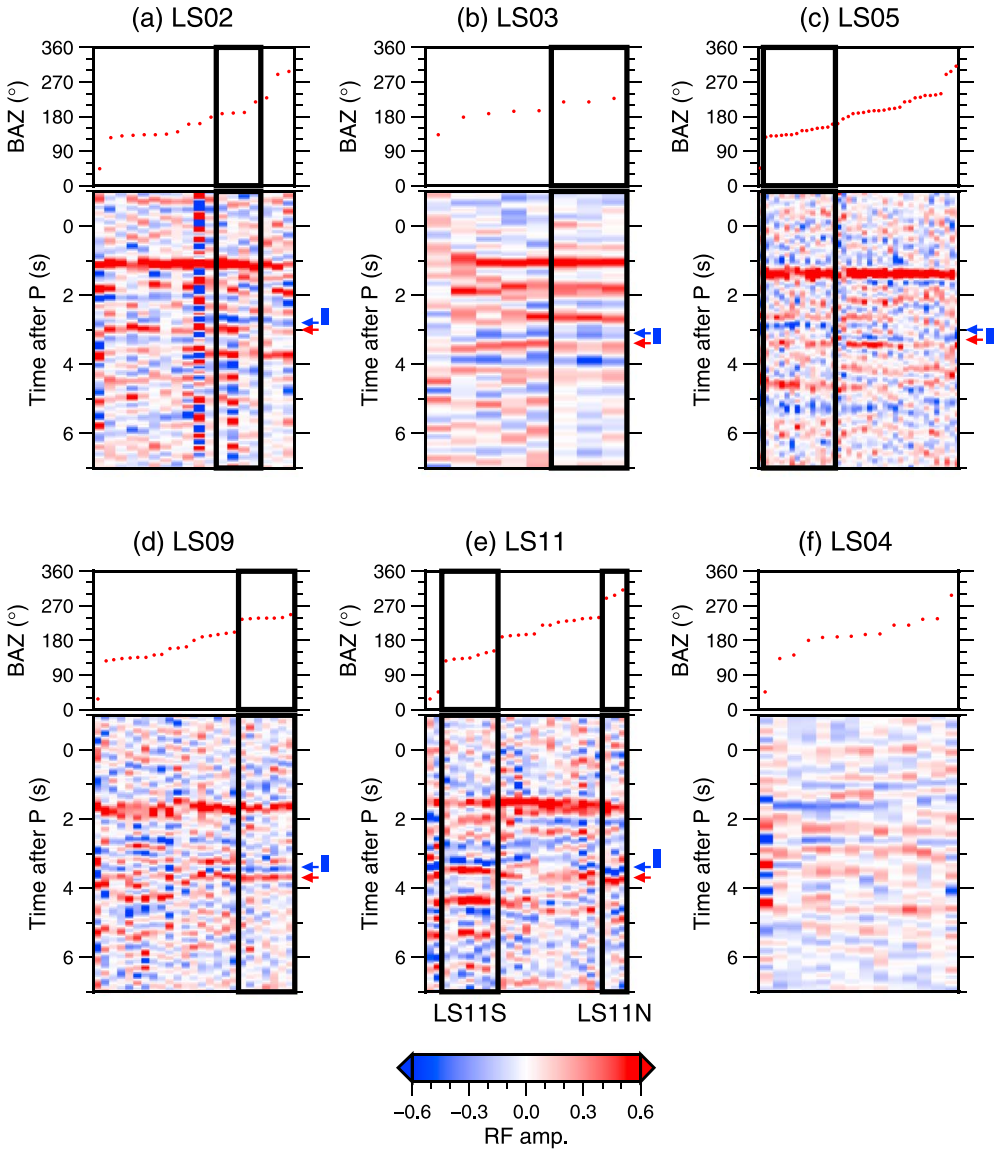

Figure 2. Radial receiver functions (RFs) (bottom row) and their event back azimuths (top row) for (a–e) five OBSs with clear *P*-to-*S* conversions from the bottom of the sediment and (f) a typical OBS that does not show such clear conversions. Thick black lines enclose the RFs analyzed in this study. Red and blue arrows denote *PsL*+ and *PsL*− phases, respectively. Blue bars represent depths of subducting plate interface [*Akuhara and Mochizuki*, 2015], where time-depth conversion was conducted using a previous tomography model [*Akuhara et al.*, 2013].

Although resultant radial RFs show coherent signals over traces at each station, they are difficult to interpret at first sight. This complexity is most likely due to unconsolidated sediment covering the seafloor. Out of all 32 OBSs, we selected five OBSs, LS02, LS03, LS05, LS09, and LS11, whose RFs exhibit clear positive peaks 1–2 s after direct *P* arrivals (Figures 2a–2e; a typical OBS not showing such peaks is shown in Figure 2f for reference). We interpret this positive peak as a *P*-to-*S* conversion from the bottom of the sediment layer. Another common feature among the five OBSs is the absence of positive peaks at zero-lag time. Low seismic velocity of the sediment causes near-vertical incidence of the direct *P* phase, leading to no energy on horizontal components. Several coherent phases can be seen after the arrivals of the *P*-to-*S* conversions that may be interpreted as sediment-related reverberations or *P*-to-*S* conversions from deeper interfaces. We find successive negative and positive phases (blue and red arrows in Figures 2a–2e) near the arrival times of *P*-to-*S* conversions from the subducting plate interface that is expected from the established tomography model [*Akuhara et al.*, 2013]. The short time intervals between these phases (<1 s) suggest a thin LVZ along the

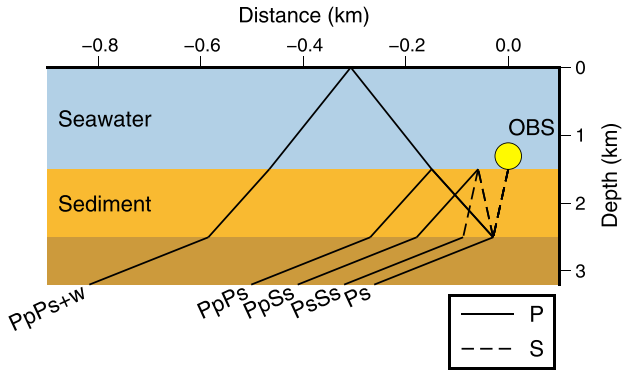

Figure 3. Definition of phase names used in *H*-κ stacking method. The raypaths are calculated using typical sediment velocities (1.7 km/s and 0.43 km/s for *P* and *S* wave velocities, respectively) and a ray parameter of 0.07 s km^{-1}. Note horizontal exaggeration.

subducting plate interface. However, we cannot and should not judge whether this prediction is correct or not before identifying multiple phases from the sediment layer [*Kawakatsu and Abe*, 2016]. Hereinafter, these negative and positive phases are referred to as *PsL*− and *PsL*+ phases, respectively.

In the subsequent sections, we first estimate the sediment layer properties using the *H*-κ stacking method [*Zhu and Kanamori*, 2000] to confirm that the *PsL*− and *PsL*+ phases do not originate from the sediment layer beneath the seafloor, but from the LVZ along the subducting plate interface (section 3). Then we conduct RF waveform inversion to investigate the LVZ properties (section 4). We set a limited back azimuth bin to be analyzed for each LS02, LS03, LS05, and LS09, and two back azimuth bins for LS11 (hereafter we refer to these two bins as LS11N and LS11S and use these terms as station names). We located these back azimuth bins where the *PsL*− and *PsL*+ phases have relatively strong amplitudes (Figure 2). Throughout this paper, we only consider 1-D layered isotropic structure and second-order features such as dipping interface and anisotropy will be neglected for simplicity, although we find that the *PsL*− and *PsL*+ phases show a moveout pattern that is typical of landward dipping interface for some stations (e.g., the *PsL*− and *PsL*+ phases arrive earlier for LS11S than LS11N).

3. Estimation of Sediment Properties by *H*-κ Stacking Method

3.1. Methodology

We applied the *H*-κ stacking analysis [*Zhu and Kanamori*, 2000] to investigate properties of the sediment layer beneath the seafloor. In this method, thickness, h, and V_p/V_s ratio, κ, of a homogeneous layer are determined via grid search so that theoretical timings of conversion and reflection phases can yield constructive interference. In addition to commonly used three phases, *Ps*, *PpPs*, and *PpSs*, we used two more phases, *PsSs* and *PpPs* + *w*, which tend to be dominant on OBS records (see Figure 3 for the definition of these phase names). The delay times of these phases from a direct *P* wave can be expressed as follows:

$$\begin{aligned}
\Delta T_{Ps} &= h\left(\sqrt{\left(\frac{\kappa}{V_p}\right)^2 - p^2} - \sqrt{\frac{1}{V_P^2} - p^2}\right),\\
\Delta T_{PpPs} &= h\left(\sqrt{\left(\frac{\kappa}{V_p}\right)^2 - p^2} + \sqrt{\frac{1}{V_p^2} - p^2}\right),\\
\Delta T_{PpSs} &= 2h\sqrt{\left(\frac{\kappa}{V_p}\right)^2 - p^2},\\
\Delta T_{PsSs} &= h\left(3\sqrt{\left(\frac{\kappa}{V_p}\right)^2 - p^2} - \sqrt{\frac{1}{V_p^2} - p^2}\right),
\end{aligned} \tag{1}$$

and

$$\Delta T_{PpPs+w} = h\left(\sqrt{\left(\frac{\kappa}{V_p}\right)^2 - p^2} + \sqrt{\frac{1}{V_p^2} - p^2}\right) + \tau.$$

In these equations, V_p, p, and τ represent the *P* wave velocity of the sediment layer, ray parameter, and two-way traveltime within the water layer, respectively. We assumed V_p to be 1.7 km/s [*Hamilton*, 1979], so h and κ were unknown parameters.

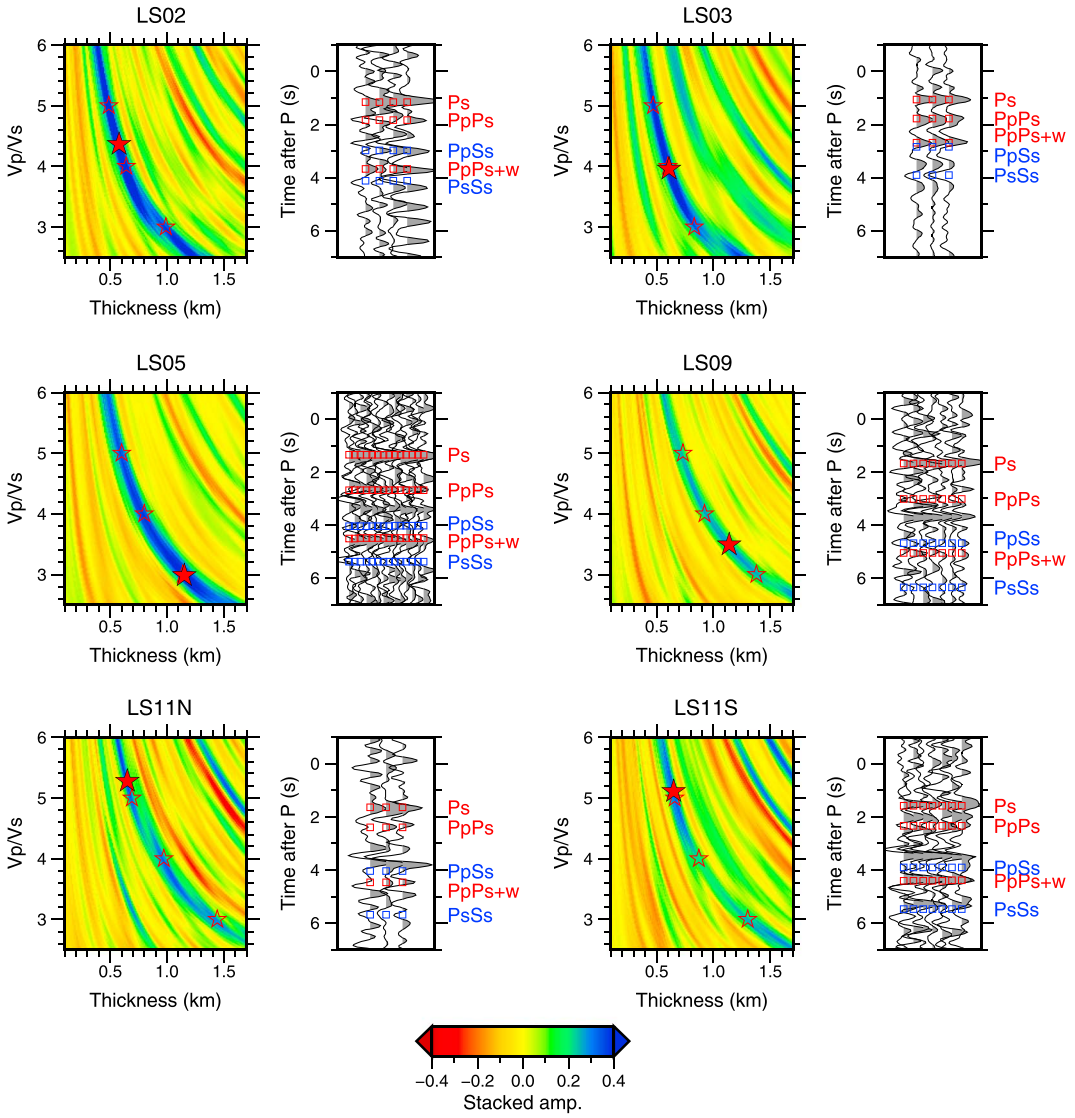

Figure 4. Results of *H*-κ stacking analysis. (left column) The stacked amplitudes in *H*-κ spaces. Red solid and open stars on the panels indicate the best sediment model predicted by the maximum amplitudes and additional models with fixed V_p/V_s values, respectively. (right column) The receiver functions used in the analysis. Red and blue squares denote predicted arrival of sediment-related phases by the best model with positive and negative polarities, respectively.

Using the equations in (1), we performed a grid search on *h*-κ space to find the maximum of the stack function:

$$s = \sum_{i=1}^{N} \left\{ w_1 r_i(\Delta T_{Ps}) + w_2 r_i(\Delta T_{PpPs}) - w_3 r_i(\Delta T_{PpSs}) - w_4 r_i(\Delta T_{PsSs}) + w_5 r_i(\Delta T_{PpPs+w}) \right\}, \quad (2)$$

where $r_i(t)$ represents a receiver function of the ith trace out of N traces and $w_1, w_2, \cdots, w_5$ represent weighting factors assigned for each phase type. In this study, we set $w_1 = 0.5$, $w_2 = w_3 = 0.05$, and $w_4 = w_5 = 0.2$ so that the phases with larger expected amplitudes have more significant influence on the estimation.

3.2. Results

Figure 4 shows the results of the *H*-κ stacking analysis for each OBS. Relatively large stacked amplitudes define a hyperbola-like curve in *h*-κ space, which is dominated by *Ps* phases. Two different data sets from a single OBS (LS11S and LS11N) produce similar results, suggesting the stability of our analysis. The

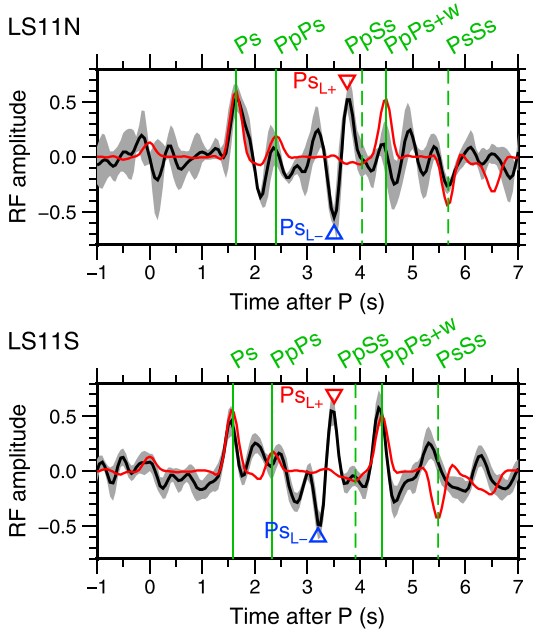

Figure 5. Comparison of observed and synthetic receiver functions (RFs) for LS11N and LS11S. Synthetic RFs (red traces) are computed using three-layered model composed of water, sediment, and half-space layer, where sediment layer is based on the best results of H-κ stacking analysis. Stacked observed RFs are shown as black traces with 2σ standard error shown by gray shaded area. Green solid and dashed lines represent predicted arrivals of positive and negative phases, respectively. Blue and red triangles denote major unmodeled phases that we interpret as *P*-to-*S* conversion phases from a low-velocity zone along subducting plate interface, i.e., *PsL*− and *PsL*+ phases.

estimated thickness and V_p/V_s ratio by the maximum stacked amplitudes vary considerably among OBSs: the estimated thickness ranges from 0.6 km to 1.1 km, and the V_p/V_s ratio from 3.0 to 5.3. Such variations can be reasonable, considering that the separation distance of OBSs (~20 km) is larger than or comparable with the typical length scale in undulation of the sediment thickness in this region (~10 km) [*Tsuji et al.*, 2015]. A previous reflection survey identified clear reflectors at the bottom of the fore-arc basin sediment in this region, and the reflectors were characterized by 0.5–2.0 s two-way traveltime from the seafloor [*Tsuji et al.*, 2015]. This two-way traveltime corresponds to a 0.4–1.7 km thickness if we assume its *P* wave velocity to be 1.7 km/s, roughly consistent with the thickness we estimated. V_p/V_s ratio of the sediment layer also may vary, in response to the variation of the thickness [*Hamilton*, 1979]. Unfortunately, no study has reported the V_p/V_s ratio of the sediment layer in our study area. The V_p/V_s ratio of 2.85–3.67 has been estimated off the Shikoku Island but still 200–300 km away from our study area [*Takahashi et al.*, 2002]: our estimated values are comparable or somewhat higher than this estimation.

Based on the above result of H-κ stacking, we then computed synthetic RFs using a three-layer model composed of water, sediment, and half-space layers in order to compare them with the observed RFs. Velocities of the half-space layer were given by the tomography model [*Akuhara et al.*, 2013], and thickness and velocities of the sediment layer were given by the results of the H-κ stacking analysis. The synthetic RFs were produced by first calculating both radial and vertical synthetic waveforms using the propagator matrix method [*Haskell*, 1953]. Then, we computed radial RFs from these two components using IWLF and low-pass filter to 4.0 Hz as described in section 2. Observed RFs were stacked in the frequency domain using the frequency-dependent uncertainties as weighting factors [*Park and Levin*, 2000]. Standard errors of the stacked RFs were estimated by bootstrap sampling 2000 times [*Efron*, 1982].

The resultant synthetic RFs reproduce observed amplitudes of the direct *P* wave arrivals, *Ps* phases, and *PpPs* phases well for most stations, while the *PsL*− and *PsL*+ phases are not recovered by this experiment (Figures 5 and S2). Thus, we interpret that the *PsL*− and *PsL*+ phases are *P*-to-*S* conversions originating from the top and bottom of the thin LVZ along the subducting plate interface. Since the *PsL*− and *PsL*+ phases can be seen for all OBSs deployed over a zone ~100 km wide, we postulate that the LVZ is a dominant structure of the subducting plate interface, rather than local heterogeneity. Our H-κ stacking analysis might suffer from a trade-off between thickness and V_p/V_s ratio, considering the dominant hyperbola-like curves by *Ps* phases in Figure 4. We, therefore, tested three additional sediment models with V_p/V_s ratio of 3.0, 4.0, and 5.0 (Figure 4, red open stars), aside from the model predicted by the maximum stacked amplitudes (Figure 4, red solid stars). The results show that all of three sediment models fail to reproduce both *PsL*− and *PsL*+ phases at all stations (Figure S2), further supporting our interpretation.

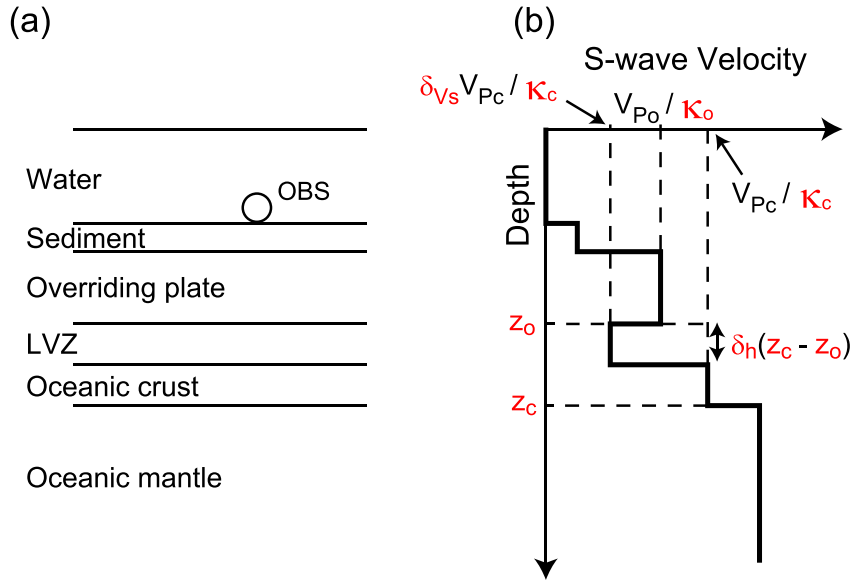

Figure 6. Schematic illustration of layered structure with depth-velocity diagrams assumed in our inversion. Six parameters shown in red color (z_o, z_c, κ_o, κ_c, δ_h, and δ_{V_s}) are model parameters. The other parameters were fixed using prior information. *P* wave velocities of the overriding plate and the oceanic crust are denoted by V_{P_o} and V_{P_c}, respectively. Note that *S* wave velocity and thickness of the low-velocity zone are expressed by $\delta_{V_s}V_{P_c}/\kappa_c$ and $\delta_h(z_c - z_o)$, respectively.

4. Receiver Function Inversion Analysis

4.1. Methodology

Our inversion searches for 1-D isotropic layered models that predict the observed RFs well. We assume that the 1-D-layered structure is composed of six homogeneous layers including the bottom half-space: i.e., the seawater, sediment, overriding plate, LVZ along the plate interface, oceanic crust, and oceanic mantle, from its top to bottom (Figure 6). To fully describe the model, we need *P* and *S* wave velocities (V_p and V_s, respectively), density (ρ), and thickness (h) for each layer. Inverting all parameters without any prior knowledge, however, seems unrealistic, considering the nonuniqueness of RF inversion [*Ammon et al.*, 1990]. Instead, we limited the number of model parameters and search ranges by exploiting prior information from the results of the *H*-κ stacking analysis and other previous studies as follows. Note that we posed relatively loose restriction on LVZ parameters as they were the main targets.

For the water layer, *P* wave velocity and density were fixed at typical values (V_p=1.5 km/s and ρ=1.0 g/cm^3). The thickness was also fixed at the OBS depths, which had been measured by acoustic ranging. No unknown parameters were assigned to this layer. For the sediment layer, all parameters (h, V_p, V_s, and ρ) were fixed and the values were exported from the best model of the *H*-κ stacking analysis. No unknown parameters were assigned to this layer, like the water layer. For overriding and oceanic crust layers, we treated the layer bottom depths (z_o and z_c, respectively) and V_p/V_s ratio (κ_o and κ_c, respectively) as unknown parameters (Figure 6). The search range of z_o and z_c are set to ±2 km wide around the depth of the plate interface and the oceanic Moho, respectively, which were estimated previously [*Akuhara and Mochizuki*, 2015]. Search ranges of κ_o and κ_c are 1.6 to 1.8 and 1.6 to 2.0, respectively. We extracted *P* wave velocity from the tomography model [*Akuhara et al.*, 2013]. In addition, we specified density using an empirical relationship with *P* wave velocity [*Birch*, 1961] as follows:

$$\rho = 0.328V_p + 0.613 \tag{3}$$

We parameterized the LVZ layer in two special parameters, δ_h and δ_{V_s}, which represent the percentage of thickness and *S* wave velocity of this layer relative to those of the oceanic crust layer, respectively. With this treatment, we could allow the LVZ to reside around the plate interface depth. Note that the absolute thickness and *S* wave velocities of this layer are given by $\delta_h(z_c - z_o)$ and $\delta_{V_s}V_{Pc}/\kappa_c$,

respectively, where V_{pc} represents P wave velocity of the oceanic crust (Figure 6). Their search ranges were set at 0–50% for δ_h and 10–80% for δ_{V_s}. The density was specified using the empirical relationship in ((3)). For the oceanic mantle, all parameters were fixed at typical values (V_p=8.1 km/s, V_s=4.7 km/s, and ρ=3.4 g/cm^3).

To find the optimum parameter set, we employed the neighborhood algorithm, a variant of Monte Carlo simulation [*Sambridge*, 1999]. The algorithm first randomly generates 4000 samples in the multidimensional parameter space and evaluates misfit values of these samples. At every iteration step, the algorithm selects top 20 samples with the lowest misfit values out of all samples so far generated. Then, two new samples are randomly generated at the proxy of each selected sample. We repeated this process 400 times to generate 20000 models.

We defined the misfit values based on cross-correlation coefficients as follows [*Frederiksen et al*., 2003]:

$$\text{misfit} = 1 - \frac{\int_t u_{\text{syn}}(t)\cdot u_{\text{obs}}(t)\mathrm{d}t}{\sqrt{\int_t u_{\text{syn}}^2(t)\mathrm{d}t}\cdot\sqrt{\int_t u_{\text{obs}}^2(t)\mathrm{d}t}} \tag{4}$$

where u_{syn} and u_{obs} represent synthetic and observed RFs, respectively. We used 8 s long time windows starting 1 s before the direct P wave arrival to the misfit measurements. This window length was chosen so that the *PsSs* phase could be included.

4.2. Results

Our inversion produced well-converged misfit value after the 400 iteration steps (Figure S3). Considering uncertainties of observed RFs, reporting ranges of the parameters that can explain observed waveforms well is more important rather than reporting only the best fit result. We, therefore, selected "preferable" models out of all 20000 models using two criteria. As the first criterion, we employed a threshold value of misfit values for each OBS. We defined the threshold value as the fourth lowest misfit value (i.e., 0.1 percentile) of the 4000 random models generated at the first iteration step of the inversion (Figure S3). In other words, any model with misfit values lower than this threshold is expected to show better waveform fit than random samples with probability 0.999. The second criterion was introduced to assure good waveform fits for *PsL*− and *PsL*+ phases. For this purpose, we selected models that predict both *PsL*− and *PsL*+ phases within ±0.15 s ranges around the peaks of the observed *PsL*− and *PsL*+ phases. Note that the range of 0.15 s corresponds to a quarter of the dominant period of the observed RFs.

Figure 7 shows the ensembles of S wave velocity profiles of the extracted preferable models. As we expected, the velocity profiles show thin LVZs near the plate interface depths. Their velocities are significantly lower than the upper limit we imposed for the inversion (i.e., 80% of the oceanic crust velocity). The velocity profiles of LS11N and LS11S are consistent, except for the LVZ depth. This difference most likely represents the landward dipping interface as seen from the moveout patterns of the *PsL*− and *PsL*+ phases (Figure 2e). We also see that the synthetic waveforms of the preferable models reproduce the observed *PsL*− and *PsL*+ phases well (Figure 8). Synthetic seismograms calculated for pure elastic (i.e., no attenuation) structures tend to overestimate amplitudes of some of later phases (e.g., *PpPs* + *w* for LS09 and LS11N, and *PsSs* for LS09 and LS11S). We attribute this partly to the topography variations of the sediment-basement interface in the fore-arc accretionary prism [*Tsuji et al*., 2015] (particularly severe for *PpPs* + *w* that has long horizontal leg (Figure 3)), and partly to the strong attenuation in the sediment layer [*Hino et al*., 2015].

The preferable models indicate positive correlation, or a trade-off, between S wave velocity and thickness of the LVZs, which is reasonably mitigated with constraints from the amplitudes of the *PsL*− and *PsL*+ phases (Figure 9). Here we define preferable ranges of the LVZ parameters so that all preferable models are included in the ranges (red rectangles in Figure 9). The averaged preferable ranges of all stations are 0.7–2.4 km/s for S wave velocity and 0.2–1.2 km for thickness (Figure 10). We also conducted the waveform inversion and evaluated the preferable parameter ranges using the different sediment models (i.e., red open stars in Figure 4). Consequently, we find that our results do not change drastically (Figure S4). This seems reasonable from Figure S2, where any sediment models do not produce sediment-related phases overprinting the *PsL*− and *PsL*+ phases.

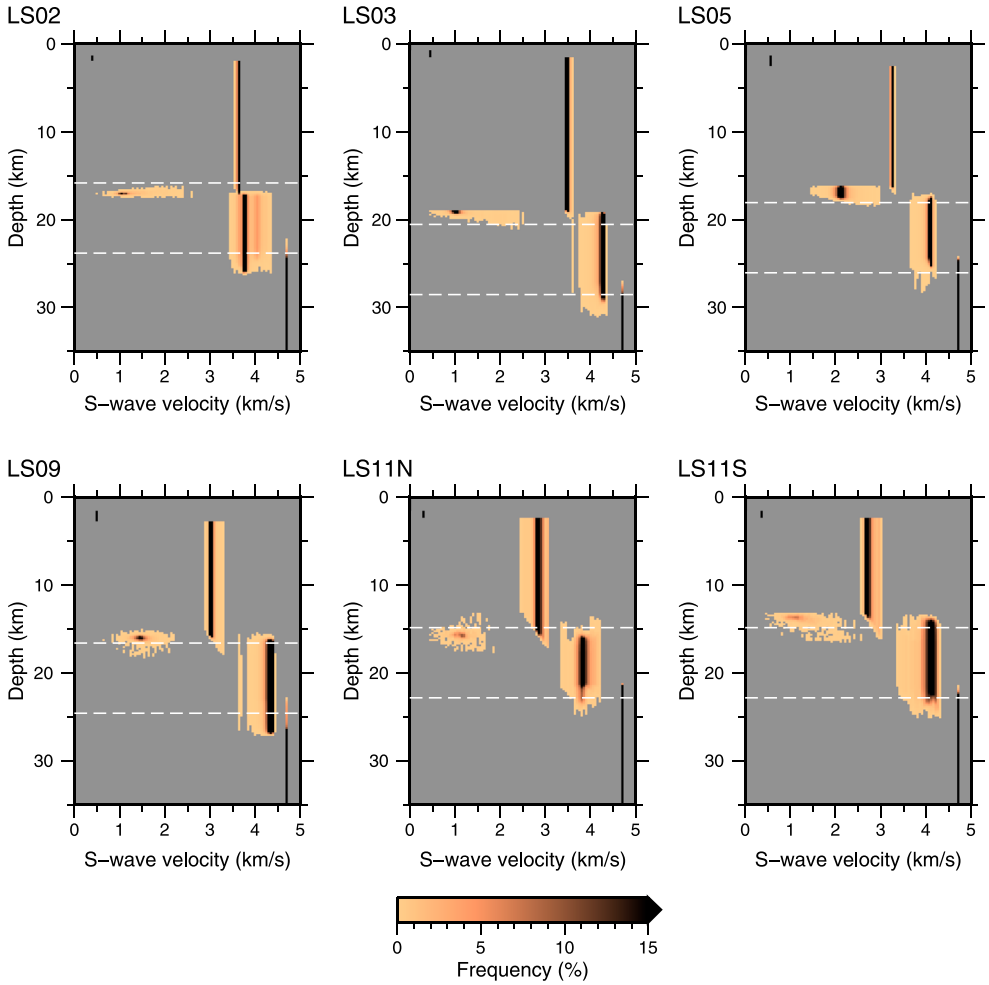

Figure 7. Ensemble of preferable *S* wave velocity structures obtained by inversion analysis (brown color). White dashed lines denote depths of the plate interface and the oceanic Moho estimated by *Akuhara and Mochizuki* [2015]. The area not sampled by the preferable models is masked by gray.

5. Fluid-Rich Subducting Sediment Layer Along the Plate Interface

We have characterized an LVZ along the plate interface beneath an offshore region at seismogenic zone depths. The averaged preferable ranges are 0.7–2.4 km/s for *S* wave velocity and 0.2–1.2 km for thickness (Figure 10). A number of RF studies (and also tomographic analyses) have identified LVZs along subducting oceanic plates in various subduction zones and interpreted them as hydrous oceanic crust [*Bostock*, 2013, and references therein]. Our estimated thickness, however, is too thin to be interpreted as the whole oceanic crust that should be ~7 km thick [e.g., *Kodaira et al*., 2006], or the upper oceanic crust that is ~3 km thick [*Hansen et al*., 2012].

We interpret that the LVZ reflects a thin fluid-rich sediment layer between subducting plate and overriding plate (i.e., along the subducting plate interface). Similar interpretations have been made through active source seismic surveys conducted in our study area based on intense *P*-to-*P* reflection phases from the plate interface [*Kodaira et al*., 2002]. Although the thickness of such a subducting sediment layer has not been estimated at the depth where we identified the LVZ (15–20 km depth), it has been estimated to be 1–2 km before the subduction [*Ike et al*., 2008] and at shallower subduction depths ($<$ 10 km) [*Bangs et al*., 2009; *Kamei et al*., 2012; *Tsuji et al*., 2014]. We consider that a similar fluid-rich sediment layer extends beneath our study area, possibly with its thickness tapering off during the subduction.

The obtained *S* wave velocities, 0.7–2.4 km/s, are suitable for water-saturated sedimentary rocks: for example, water-saturated sandstone under effective pressure of 30–40 MPa can explain the LVZ velocities according to

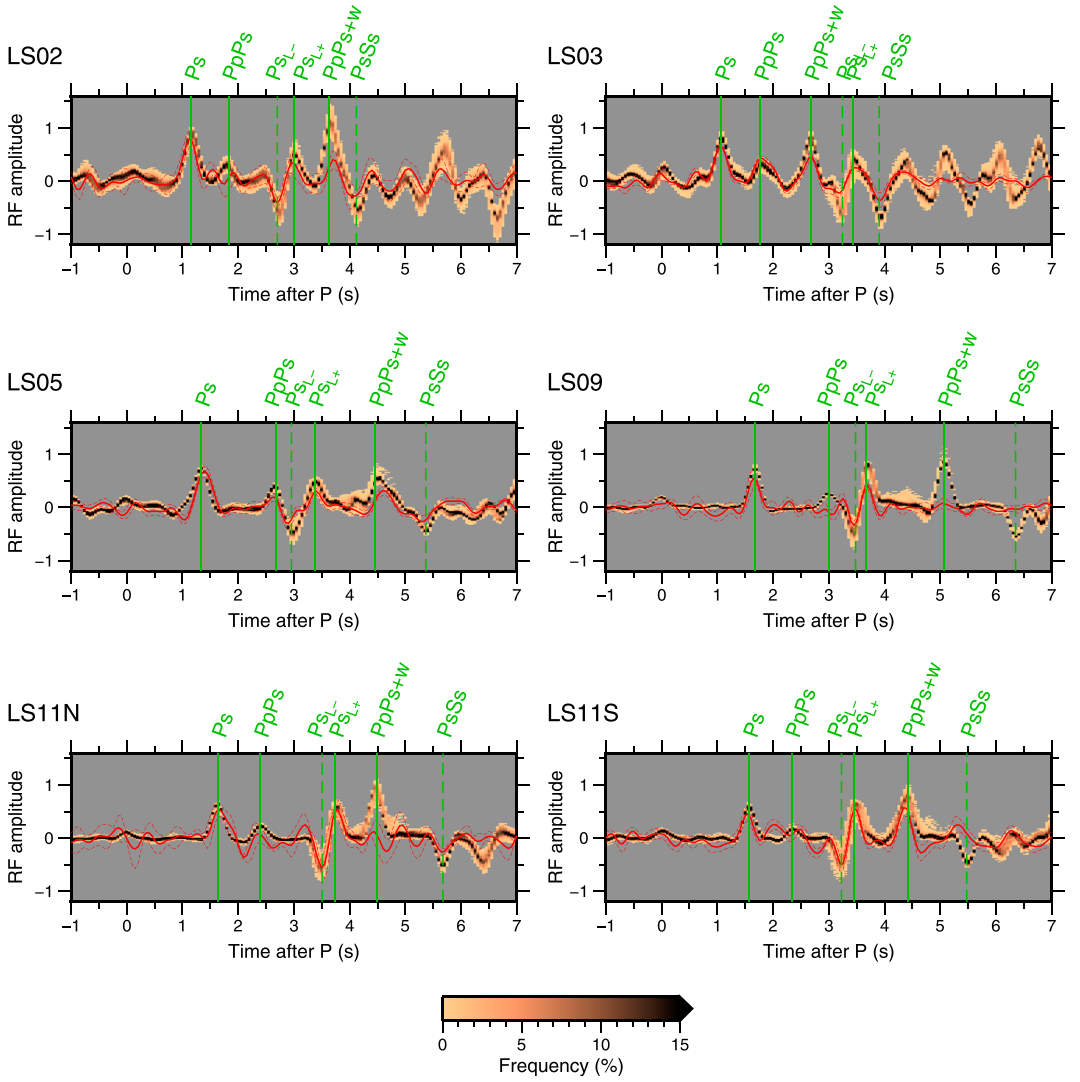

Figure 8. Ensemble of synthetic receiver functions (RFs) calculated with preferable models obtained by inversion analysis (brown color). Red solid and dashed traces show observed RFs and their 2σ standard error, respectively. Green solid and dashed lines represent predicted arrivals of positive and negative phases, respectively. The area where no synthetic traces pass is masked by gray.

laboratory experiments [*Mavko et al.*, 2009, and references therein] (Figure 10). Note that the effective pressure of 30–40 MPa corresponds to ~10–20% of the vertical load from the overriding plate at the LVZ depth. It also corresponds to the overpressure ratio [*Screaton et al.*, 2002] of ~0.7–0.9, if simply assuming lithostatic pressure equal to the vertical load and pore pressure equal to the difference between the lithostatic and the effective pressures. This overpressure ratio is somewhat lower than that reported for the shallower subduction depth where very low frequency earthquakes occur [*Tsuji et al.*, 2014]. Although we only present sandstone as an example here, other types of sedimentary rock (e.g., mudstone) can be a plausible material of the LVZ. Moreover, lower velocity may be explained by high degree of clay content [*Eberhart-Phillips et al.*, 1989].

As incoming sediment has been considered fully dehydrated at the early stage of subduction [*Hyndman and Peacock*, 2003], we infer that the low-velocity sediment layer is a fluid path way rather than a fluid source. The existence of fluid pathway that transport fluid from deep to shallow along the subducting Philippine Sea Plate has been suggested by the heat flow modeling [*Spinelli and Wang*, 2008] and by the lithium isotope ratio in submarine mud volcano fluid [*Nishio et al.*, 2015].

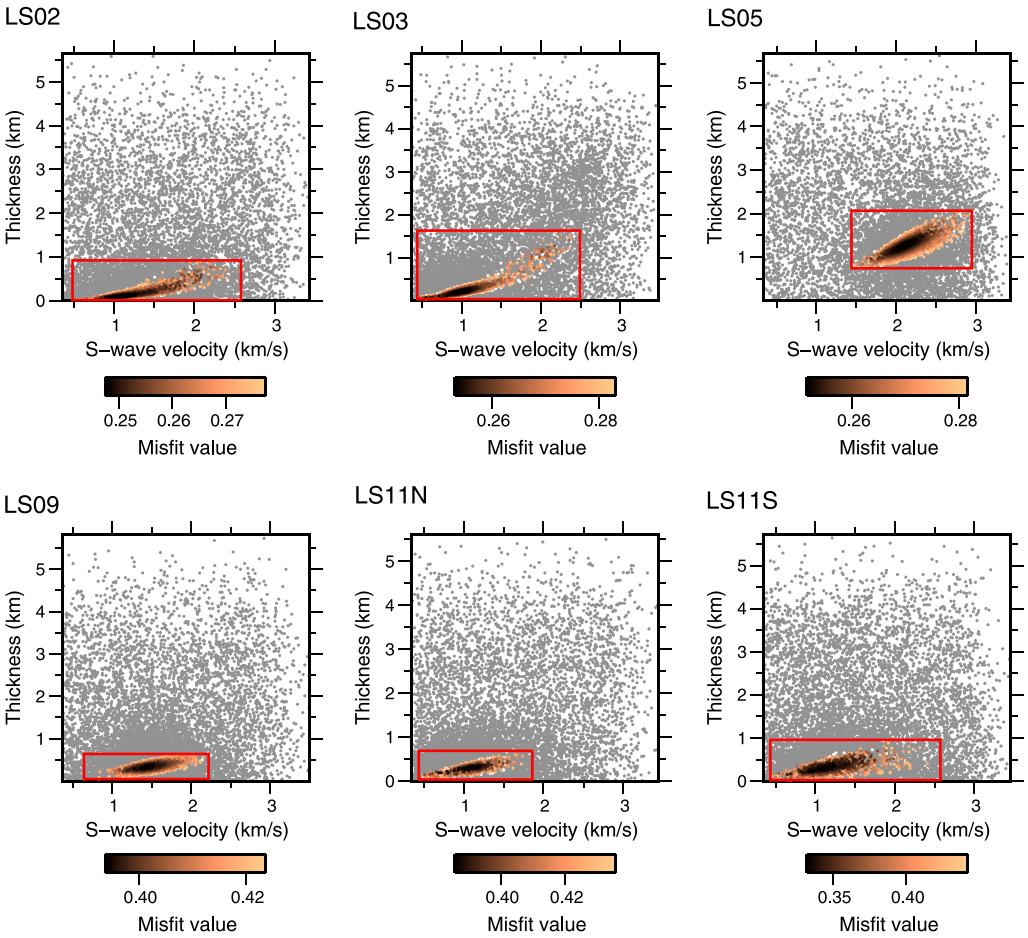

Figure 9. Misfit value distributions against *S* wave velocity and thickness of the low-velocity zone (LVZ). Brownish color is given for preferable models, while the other models are shown by gray dots. Red lines denote preferable ranges of *S* wave velocity and thickness of the LVZ.

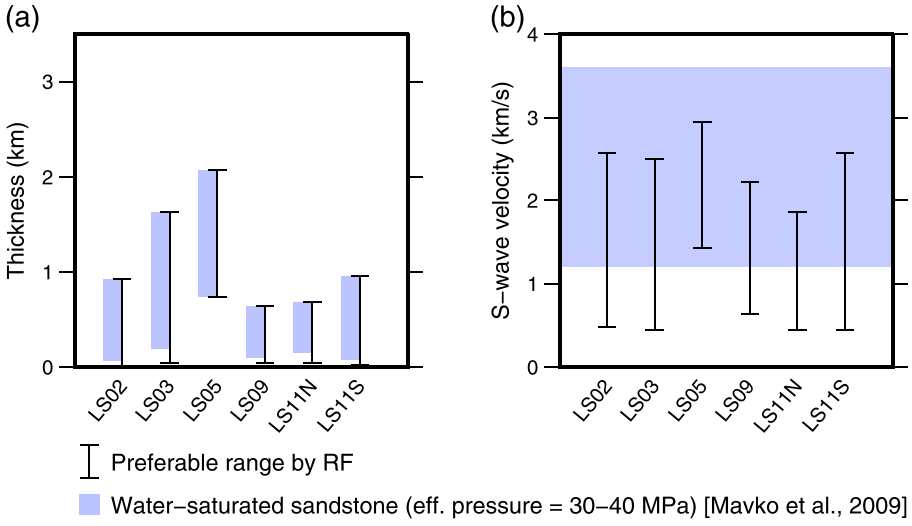

Figure 10. Summary of low-velocity zone (LVZ) parameters, (a) thickness and (b) *S* wave velocity, obtained by this study. Vertical bars denote preferable ranges of the parameter for each station. Blue shaded area in Figure 10b represents *S* wave velocity range of sandstone reported by laboratory measurements [*Mavko et al.,* 2009], and the area in Figure 10a shows the corresponding thickness range of preferable models.

Similar thin LVZs have been revealed through active source seismic surveys at seismically locked zones of other subduction zones based on intense *P*-to-*P* reflection phases from the plate interface [*Nedimović et al*., 2003; *Mochizuki et al*., 2005; *Bell et al*., 2010; *Li et al*., 2015], suggesting that subducting fluid-rich sediment layers are a ubiquitous feature of subduction zones. *Nedimović et al*. [2003] and *Li et al*. [2015] have estimated the thicknesses of the LVZs at Cascadia and Alaska subduction zones to be <2 km and 100–250 m, respectively, roughly consistent with our results. They have also revealed abrupt change in the thickness along the dip direction: the LVZs become thicker ($>$ 2 km) at greater depth, downdip of seismogenic plate interfaces. Most RF studies using on-land data have obtained thicker LVZs which are interpreted as the hydrated oceanic crust [*Bostock*, 2013, and references therein]. The discrepancy in the LVZ thickness reported by our study and those on-land-based studies may reflect the depth-dependent properties of the megathrusts [*Nedimović et al*., 2003; *Li et al*., 2015]. Otherwise, analyzing RFs at high frequency using on-land stations might help detect thinner low-velocity sediment layers.

6. Conclusion

Recent progress in analysis methods has opened opportunities to conduct high-frequency RF analysis using OBS records. In this study, we extracted RFs from OBSs deployed off the Kii Peninsula, southwest Japan, using low-pass filter of <4 Hz, removing water reverberations from vertical component records. We first interpreted the observed RFs in terms of sediment-related conversions and reflections using the H-κ stacking method and found that deeper structures are required to explain some prominent phases. The arrival times of these phases roughly correspond to the depth of the subducting plate interface, suggesting the presence of an LVZ along the plate interface. We constrained the LVZ properties by RF waveform inversion to reveal that the LVZ is characterized by thin thickness and low seismic velocities. We interpreted this feature as a fluid-rich incoming sediment.

Nowadays, large-scale scientific projects involving passive seismic observations at offshore sites have been launched or are undergoing at subduction zones worldwide [e.g., *Scherwath et al*., 2011; *Kaneda*, 2014; *Toomey et al*., 2014; *Harris et al*., 2016]. Unfortunately, the application of RF analysis to such offshore data are limited to date [e.g., *Akuhara and Mochizuki*, 2015; *Janiszewski and Abers*, 2015; *Akuhara et al*., 2016; *Audet*, 2016]. Our analysis method has overcome severe problem specific to OBS data by taking multiple phases within seawater and sediment layers into consideration. Since the RF methods have different sensitivity from traditional active source seismic surveys, we believe that applying similar analysis to other regions helps us acquire advanced knowledge about the physical properties around megathrust faults.

Acknowledgments

We are grateful to Michael Bostock for insightful feedback on an early draft. We also appreciate Jeffrey Park and an anonymous reviewer for their constructive comments and suggestions. This work was supported by JSPS KAKENHI grant 26-10221. We used The Generic Mapping Tools [*Wessel and Smith*, 1991] for drawing figures and the computer package NA (Neighborhood Algorithm) released by the AuScope Inversion Laboratory for inversion analysis. Teleseismic waveform data used in this study are available from https://www.researchgate.net/publication/317597078_Teleseismic_waveforms.

References

Akuhara, T., and K. Mochizuki (2015), Hydrous state of the subducting Philippine Sea plate inferred from receiver function image using onshore and offshore data, *J. Geophys. Res. Solid Earth*, *120*, 8461–8477, doi:10.1002/2015JB012336.

Akuhara, T., K. Mochizuki, K. Nakahigashi, T. Yamada, M. Shinohara, S. Sakai, T. Kanazawa, K. Uehira, and H. Shimizu (2013), Segmentation of the V_P/V_S ratio and low-frequency earthquake distribution around the fault boundary of the Tonankai and Nankai earthquakes, *Geophys. Res. Lett.*, *40*, 1306–1310, doi:10.1002/grl.50223.

Akuhara, T., K. Mochizuki, H. Kawakatsu, and N. Takeuchi (2016), Non-linear waveform analysis for water-layer response and its application to high-frequency receiver function analysis using OBS array, *Geophys. J. Int.*, *206*(3), 1914–1920, doi:10.1093/gji/ggw253.

Ammon, C. J., G. E. Randall, and G. Zandt (1990), On the nonuniqueness of receiver function inversions, *J. Geophys. Res.*, *95*(B10), 15,303–15,318, doi:10.1029/JB095iB10p15303.

Ando, M. (1975), Source mechanisms and tectonic significance of historical earthquakes along the Nankai Trough, Japan, *Tectonophysics*, *27*(2), 119–140, doi:10.1016/0040-1951(75)90102-X.

Audet, P. (2016), Receiver functions using OBS data: Promises and limitations from numerical modelling and examples from the Cascadia initiative, *Geophys. J. Int.*, *205*(3), 1740–1755, doi:10.1093/gji/ggw111.

Audet, P., M. G. Bostock, N. I. Christensen, and S. M. Peacock (2009), Seismic evidence for overpressured subducted oceanic crust and megathrust fault sealing, *Nature*, *457*(7225), 76–78.

Bangs, N. L. B., G. F. Moore, S. P. S. Gulick, E. M. Pangborn, H. J. Tobin, S. Kuramoto, and A. Taira (2009), Broad, weak regions of the Nankai megathrust and implications for shallow coseismic slip, *Earth Planet. Sci. Lett.*, *284*(1–2), 44–49, doi:10.1016/j.epsl.2009.04.026.

Bell, R., R. Sutherland, D. H. N. Barker, S. Henrys, S. Bannister, L. Wallace, and J. Beavan (2010), Seismic reflection character of the Hikurangi subduction interface, New Zealand, in the region of repeated Gisborne slow slip events, *Geophys. J. Int.*, *180*(1), 34–48, doi:10.1111/j.1365-246X.2009.04401.x.

Birch, F. (1961), The velocity of compressional waves in rocks to 10 kilobars: 2, *J. Geophys. Res.*, *66*(7), 2199–2224, doi:10.1029/JZ066i007p02199.

Bostock, M. G. (2013), The Moho in subduction zones, *Tectonophysics*, *609*, 547–557, doi:10.1016/j.tecto.2012.07.007.

Eberhart-Phillips, D., D.-H. Han, and M. D. Zoback (1989), Empirical relationships among seismic velocity, effective pressure, porosity, and clay content in sandstone, *Geophysics*, *54*(1), 82–89, doi:10.1190/1.1442580.

Efron, B. (1982), *The Jackknife, the Bootstrap and Other Resampling Plans*, SIAM, Philadelphia, Pa.

Frederiksen, A. W., H. Folsom, and G. Zandt (2003), Neighbourhood inversion of teleseismic *Ps* conversions for anisotropy and layer dip, *Geophys. J. Int.*, *155*(1), 200–212, doi:10.1046/j.1365-246X.2003.02043.x.

Hamilton, E. L. (1979), V_P/V_s and Poisson's ratios in marine sediments and rocks, *J. Acoust. Soc. Am.*, *66*(4), 1093–1101, doi:10.1121/1.383344.

Hansen, R. T. J., M. G. Bostock, and N. I. Christensen (2012), Nature of the low velocity zone in Cascadia from receiver function waveform inversion, *Earth Planet. Sci. Lett.*, *337-338*, 25–38, doi:10.1016/j.epsl.2012.05.031.

Harris, R., et al. (2016), Investigations of shallow slow slip offshore of New Zealand, *Eos*, *97*, doi:10.1029/2016EO048945.

Haskell, N. A. (1953), The dispersion of surface waves on multilayered media, *Bull. Seismol. Soc. Am.*, *43*(1), 17–34.

Hino, R., T. Tsuji, N. L. Bangs, Y. Sanada, J.-O. Park, R. von Huene, G. F. Moore, E. Araki, and M. Kinoshita (2015), Q_P structure of the accretionary wedge in the Kumano Basin, Nankai trough, Japan, revealed by long-offset walk-away VSP, *Earth Planets Space*, doi:10.1186/s40623-014-0175-x.

Hyndman, R. D., and S. M. Peacock (2003), Serpentinization of the forearc mantle, *Earth Planet. Sci. Lett.*, *212*(3–4), 417–432, doi:10.1016/S0012-821X(03)00263-2.

Hyndman, R. D., P. A. McCrory, A. Wech, H. Kao, and J. Ague (2015), Cascadia subducting plate fluids channelled to fore-arc mantle corner: ETS and silica deposition, *J. Geophys. Res. Solid Earth*, *120*, 4344–4358, doi:10.1002/2015JB011920.

Ike, T., G. F. Moore, S. Kuramoto, J. Park, Y. Kaneda, and A. Taira (2008), Tectonics and sedimentation around Kashinosaki Knoll: A subducting basement high in the eastern Nankai Trough, *Island Arc*, *17*(3), 358–375, doi:10.1111/j.1440-1738.2008.00625.x.

Janiszewski, H. A., and G. A. Abers (2015), Imaging the plate Interface in the Cascadia Seismogenic zone: New constraints from offshore receiver functions, *Seismol. Res. Lett.*, *86*(5), 1261–1269, doi:10.1785/0220150104.

Kamei, R., R. G. Pratt, and T. Tsuji (2012), Waveform tomography imaging of a megasplay fault system in the seismogenic Nankai subduction zone, *Earth Planet. Sci. Lett.*, *317-318*, 343–353, doi:10.1016/j.epsl.2011.10.042.

Kaneda, Y. (2014), DONET: A real-time monitoring system for megathrust earthquakes and tsunamis around southwestern Japan, *Oceanography*, *27*(2), 103, doi:10.5670/oceanog.2014.45.

Kawakatsu, H., and Y. Abe (2016), Comment on "Nature of the seismic lithosphere-asthenosphere boundary within normal oceanic mantle from high-resolution receiver functions" by Olugboji et al, *Geochem. Geophys. Geosyst.*, *17*, 3488–3492, doi:10.1002/2016GC006418.

Kawakatsu, H., and S. Watada (2007), Seismic evidence for deep-water transportation in the mantle, *Science*, *316*, 1468–1471, doi:10.1126/science.1140855.

Kim, Y., and R. W. Clayton (2015), Seismic properties of the Nazca oceanic crust in southern Peruvian subduction system, *Earth Planet. Sci. Lett.*, *429*, 110–121, doi:10.1016/j.epsl.2015.07.055.

Kimura, G., S. Hina, Y. Hamada, J. Kameda, T. Tsuji, M. Kinoshita, and A. Yamaguchi (2012), Runaway slip to the trench due to rupture of highly pressurized megathrust beneath the middle trench slope: The tsunamigenesis of the 2011 Tohoku earthquake off the east coast of northern Japan, *Earth Planet. Sci. Lett.*, *339-340*, 32–45, doi:10.1016/j.epsl.2012.04.002.

Kodaira, S., E. Kurashimo, J. Park, N. Takahashi, A. Nakanishi, S. Miura, T. Iwasaki, N. Hirata, K. Ito, and Y. Kaneda (2002), Structural factors controlling the rupture process of a megathrust earthquake at the Nankai trough seismogenic zone, *Geophys. J. Int.*, *149*(3), 815–835, doi:10.1046/j.1365-246X.2002.01691.x.

Kodaira, S., T. Iidaka, A. Kato, J. Park, T. Iwasaki, and Y. Kaneda (2004), High pore fluid pressure may cause silent slip in the Nankai Trough, *Science*, *304*, 1295–1298, doi:10.1126/science.1096535.

Kodaira, S., T. Hori, A. Ito, S. Miura, G. Fujie, J. Park, T. Baba, H. Sakaguchi, and Y. Kaneda (2006), A cause of rupture segmentation and synchronization in the Nankai trough revealed by seismic imaging and numerical simulation, *J. Geophys. Res.*, *111*, B09301, doi:10.1029/2005JB004030.

Li, J., D. J. Shillington, A. Bécel, M. R. Nedimović, S. C. Webb, D. M. Saffer, K. M. Keranen, and H. Kuehn (2015), Downdip variations in seismic reflection character: Implications for fault structure and seismogenic behavior in the Alaska subduction zone, *J. Geophys. Res. Solid Earth*, *120*, 7883–7904, doi:10.1002/2015JB012338.

Mavko, G., T. Mukerji, and J. Dvorkin (2009), *The Rock Physics Handbook: Tools for Seismic Analysis of Porous Media*, Cambridge Univ. Press, New York.

McCrory, P. A., J. E. Constantz, A. G. Hunt, and J. L. Blair (2016), Helium as a tracer for fluids released from Juan de Fuca lithosphere beneath the Cascadia forearc, *Geochem. Geophys. Geosyst.*, *17*, 2434–2449, doi:10.1002/2015GC006198.

Mochizuki, K., et al. (2005), Intense PP reflection beneath the aseismic forearc slope of the Japan Trench subduction zone and its implication of aseismic slip subduction, *J. Geophys. Res.*, *110*, B01302, doi:10.1029/2003JB002892.

Nishio, Y., A. Ijiri, T. Toki, Y. Morono, M. Tanimizu, K. Nagaishi, and F. Inagaki (2015), Origins of lithium in submarine mud volcano fluid in the Nankai accretionary wedge, *Earth Planet. Sci. Lett.*, *414*, 144–155, doi:10.1016/j.epsl.2015.01.018.

Nedimović, M. R., R. D. Hyndman, K. Ramachandran, and G. D. Spence (2003), Reflection signature of seismic and aseismic slip on the northern Cascadia subduction interface, *Nature*, *424*(6947), 416–420, doi:10.1038/nature01840.

Park, J., and V. Levin (2016), Statistics and frequency-domain moveout for multiple-taper receiver functions, *Geophys. J. Int.*, *207*(1), 512–527, doi:10.1093/gji/ggw291.

Park, J., and V. Levin (2000), Receiver functions from multiple-taper spectral correlation estimates, *Bull. Seismol. Soc. Am.*, *90*(6), 1507–1520, doi:10.1785/0119990122.

Sambridge, M. (1999), Geophysical inversion with a neighbourhood algorithm—I. Searching a parameter space, *Geophys. J. Int.*, *138*(2), 479–494, doi:10.1046/j.1365-246X.1999.00876.x.

Scherwath, M., G. Spence, K. Obana, S. Kodaira, K. Wang, M. Riedel, J. McGuire, and J. Collins (2011), Seafloor seismometers monitor northern Cascadia earthquakes, *Eos Trans. AGU*, *92*(47), 421–422, doi:10.1029/2011EO470001.

Scholz, C. H. (1998), Earthquakes and friction laws, *Nature*, *391*, 37–42, doi:10.1038/34097.

Screaton, E., D. Saffer, P. Henry, and S. Hunze (2002), Porosity loss within the underthrust sediments of the Nankai accretionary complex: Implications for overpressures, *Geology*, *30*(1), 19–22, doi:10.1130/0091-7613(2002)030<0019:PLWTUS>2.0.CO;2.

Shibutani, T., T. Ueno, and K. Hirahara (2008), Improvement in the extended-time multitaper receiver function estimation technique, *Bull. Seismol. Soc. Am.*, *98*(2), 812–816, doi:10.1785/0120070226.

Song, T.-R. A., D. V. Helmberger, M. R. Brudzinski, R. W. Clayton, P. Davis, X. Perez-Campos, and S. K. Singh (2009), Subducting slab ultra-slow velocity layer coincident with silent earthquakes in southern Mexico, *Science*, *324*(5926), 502–506, doi:10.1126/science.1167595.

Spinelli, G. A., and K. Wang (2008), Effects of fluid circulation in subducting crust on Nankai margin seismogenic zone temperatures, *Geology*, *36*(11), 887, doi:10.1130/G25145A.1.

Takahashi, N., et al. (2002), Seismic structure of western end of the Nankai trough seismogenic zone, *J. Geophys. Res.*, *107*(B10), 2212, doi:10.1029/2000JB000121.

Toomey, D., et al. (2014), The Cascadia initiative: A sea change in seismological studies of subduction zones, *Oceanography*, *27*(2), 138–150, doi:10.5670/oceanog.2014.49.

Tsuji, T., R. Kamei, and R. G. Pratt (2014), Pore pressure distribution of a mega-splay fault system in the Nankai Trough subduction zone: Insight into up-dip extent of the seismogenic zone, *Earth Planet. Sci. Lett.*, *396*, 165–178, doi:10.1016/j.epsl.2014.04.011.

Tsuji, T., J. Ashi, M. Strasser, and G. Kimura (2015), Identification of the static backstop and its influence on the evolution of the accretionary prism in the Nankai Trough, *Earth Planet. Sci. Lett.*, *431*, 15–25, doi:10.1016/j.epsl.2015.09.011.

Wessel, P., and W. H. F. Smith (1991), Free software helps map and display data, *Eos Trans. AGU*, *72*(41), 441–441, doi:10.1029/90EO00319.

Zhao, D., Z. Huang, N. Umino, A. Hasegawa, and H. Kanamori (2011), Structural heterogeneity in the megathrust zone and mechanism of the 2011 Tohoku-oki earthquake (mw 9.0), *Geophys. Res. Lett.*, *38*, L17308, doi:10.1029/2011GL048408.

Zhu, L., and H. Kanamori (2000), Moho depth variation in southern California from teleseismic receiver functions, *J. Geophys. Res.*, *105*(B2), 2969–2980, doi:10.1029/1999JB900322.